Simulation on Three-Dimensional Shock Interactions and Aerodynamic Heating Between Body and Wing

Mingyue Lin,* Chun Wang,† Jun Peng,‡ and Zonglin Jiang§
Chinese Academy of Sciences, 100190 Beijing, People's Republic of China

https://doi.org/10.2514/1.J060473

This study investigates the flowfield patterns and distributions of surface heat flux due to interactions among three-dimensional shock waves at the junction of the body and wing of an aircraft by solving Reynolds–averaged Navier–Stokes equations at a Mach number of 10 and attack angles ranging from 5° to 20°. The results indicate that the structures of wing/body-shock interactions vary significantly with test conditions. Four types of shock interaction patterns were observed: interaction-free, type I regular, type II regular, and Mach interactions. Once the flowfield of the shock interactions had been established, aerodynamic heating loads of the wing and body were affected by the flowfield structures. Wing/body-shock interactions produced uneven heat flux distributions on the surface and caused an abnormally high heat flux at a localized position. Five profiles of the distribution of heat flux were extracted to describe its characteristics on the surface according to the position and magnitude of the peaks of the localized heat flux. Induction-related factors that led to the peaks were classified into three types: reflected shock/boundary-layer interaction, contact surface impinging, and contact surface grazing.

Nomenclature

Ma	=	Mach number
N_Z, N_X, N_Y	=	number of cells in Z, X, and Y directions
p	=	pressure, Pa
q	=	heat flux, W/m²
R	=	radius of blunt leading edge of wing, mm
Re	=	unit Reynolds number
T	=	temperature, K
X	=	local streamwise coordinate
Y	=	local wall normal coordinate
Z	=	local spanwise coordinate

Subscripts

0	=	stagnation point
∞	=	freestream

Superscript

$+$	=	nondimensionalization by the inner scales of the boundary layer

*Master's Student, State Key Laboratory of High-Temperature Gas Dynamics, Institute of Mechanics; also School of Engineering Science, University of Chinese Academy of Sciences, 100049 Beijing, People's Republic of China.

†Professor, State Key Laboratory of High-Temperature Gas Dynamics, Institute of Mechanics; also School of Engineering Science, University of Chinese Academy of Sciences, 100049 Beijing, People's Republic of China; wangchun@imech.ac.cn (Corresponding Author).

‡Ph.D. Student, State Key Laboratory of High-Temperature Gas Dynamics, Institute of Mechanics; also School of Engineering Science, University of Chinese Academy of Sciences, 100049 Beijing, People's Republic of China.

§Professor, State Key Laboratory of High-Temperature Gas Dynamics, Institute of Mechanics; also School of Engineering Science, University of Chinese Academy of Sciences, 100049 Beijing, People's Republic of China. Associate Fellow AIAA.

I. Introduction

WING/BODY structure is the typical configuration of vehicles due to its ubiquitous presence and significant effects on the aerodynamic performance [1], stealthy performance [2], and maneuvering stability of aircrafts. Therefore, extensive attention has been focused on this structure from researchers in different fields over the years.

The spatial feature of this structure is the formation of a junction, where boundary layers on wing and body develop orthogonally and interact with each other. Characterized by secondary flows, such as horseshoe vortices and corner separations, which may trigger buffet [3] and therefore impair aerodynamic performance, this kind of junction flow [4] has become one of the most troublesome problems for aircraft designers. Horseshoe vortices at the nose of the wing are caused by the separation of incoming boundary layer, which experiences the adverse pressure gradient created by the wing and rolls up to give birth to a vortex. Many authors [5,6] focused on the low frequency and large-scale bimodal behavior of this vortex. On the other hand, there is a flow separation in the corner of the wing trailing edge, namely, corner separation. Some studies [7] also have been conducted on the features of this phenomenon. Because of the complex interaction of boundary layers, flow in this corner is highly anisotropic. Some researchers [8–13] used this structure to examine the strengths and weaknesses of different turbulence models in predicting flow separation. Most of the separations concerned in these studies are low speed, even incompressible, because many experiments were conducted in water tunnels [14,15]. When flow velocity rises to supersonic or even hypersonic, shock sets up in front of the wing. Separations of boundary layer would introduce separation and reattachment shock in the flow. These secondary flow structures interact with wing shock and set up shock-wave/boundary-layer interaction (SWBLI) and shock/shock interaction (SSI) phenomenon, which induce high and localized aerodynamic loads on the surface. Owing to the existence of unstable structures such as contact surface and supersonic jet, the flowfield is inherently unsteady, which may lead to the flutter or even direct damage to the structure [16]. As a type of protrusions on the body, shape of the wing can be reduced by using simplified models [17,18], to indicate ideal or general conditions, such as sharp unswept [19–21]/swept fin (SUF/SSF) [22], semicone (SC) model, compression ramp (CR) [23–25], blunt fin (BF) [26–30], and double sharp fin (DSF) [31].

The short literature review provided above shows that majority of the investigations on three-dimensional (3-D) wing/body structure focus on the phenomenon of separation and junction flow at low-speed. For flow at high speed, especially supersonic flow, most studies concerned wing-shock/body-boundary-layer interactions;

the analysis to SSIs of the wing/body structure is few. The fuselage is always simplified to a flat plate with no body-shock existing in the flowfield. It does not imply that the issue does not make sense; on the contrary, wing-shock/body-shock interaction induces a series of complex flowfield structures and leads to a more hostile localized thermal environment [32,33]. In the available studies focusing on the phenomenon of SSI, the structure is always related to the corner flow configuration [34] by shock wave researchers, and the focus of them is the shock structure formed by the intersection of two aerodynamic surfaces, commonly in the shape of intersecting compression wedges [35–38]. Naidoo and Skews [34] conducted numerical and experimental investigations of shock interactions along simplified wing/body structure, focusing on the formation and growth of the shear layers induced by the Mach reflection. They found that the impingement of the reflected shock causes a large variation on the thickness of boundary layer. Xiang et al. [39] theoretically solved the flow parameters of SSI of the simplified wing/body structure by using the method of spatial dimension reduction [36–38]. Few studies focused on the extreme aerodynamic heating environment induced by wing-shock/body-shock interaction, which is crucial for accurately predicting thermal environment faced by the aircraft and its thermal protection systems (TPS). Therefore, there is a need to gain a deeper understanding of the flow physics of 3-D SSI of the wing/body structure, and the mechanisms of abnormal surface heat flux in the region of interaction.

In this paper, the Reynolds-averaged Navier–Stokes (RANS) equations are solved to study complex 3-D wing shock/body-shock interactions as well as wing shock/body-boundary-layer interactions in the region of wing/body junction at a Mach number of 10. Flowfield patterns and distributions of aerodynamic heating loads are simulated in different test conditions and discussed. The results indicate that flowfield structures (especially the interactions between the reflected shock and the boundary layer, contact surface impinging, and contact surface grazing) are responsible for localized peaks in heat flux. Affected by the complex flow structures of shock interactions, aerodynamic load distributions on the surface of the aircraft, especially the distributions of heat flux, are very uneven. More than one localized heat flux peak appears due to these mechanisms. According to the magnitude and position of these peaks, five profiles of heat flux distribution are identified to reflect the effects of the characteristics of the flowfield on the distribution of the aerodynamic heating load on the surface of the aircraft.

II. Mathematical and Physical Models

A. Numerical Algorithm

In the present work, the 3-D, compressible, perfect gas RANS equations were solved using a quadrilateral-grid-based finite-volume method. The equations were discretized spatially by a second-order upwind total variation diminishing (TVD) scheme with a new multidimensional polynomial interpolation framework. The nonlinear Harten–Lax–van Leer contact (HLLC) approximate Riemann solver was used to define interface fluxes with entropy and positivity conditions satisfied automatically. The minmod limiter was employed to suppress spurious oscillations near the discontinuities, and high-order accuracy was preserved away from the discontinuities. A second-order fully implicit scheme was employed to discretize the time terms. This computational code has been used and validated in the previous work by Peng et al. [40], Zhang et al. [41], and Lu et al. [42], showing excellent performance in solving hypersonic flows including shock interactions, boundary-layer separations, shock-induced combustion, etc. The two-equation realizable $k - \varepsilon$ model (RKE) [43] was implemented to represent turbulence.

B. Code Validation

A shock-wave/turbulent-boundary-layer interaction case induced by 3-D sharp fin was used to verify the flow-characteristic-capture ability and surface-heat-flux-predict accuracy of the present computation code. The experimental data of LF23 [44], together with the available RANS simulation results [45], which used negative Spalart–Allmaras (SA-NEG) turbulence model [46], were taken to compare with our numerical results. A variety of turbulence models, namely, the two-equation nonlinear(cubic) $k - \varepsilon$(CKE) [47], two-equation R-γ transition, two-equation realizable $k - \varepsilon$(RKE) [43], and one-equation Spalart–Allmaras (SA) [48], were used to represent turbulence. The simulation initial conditions were $p_\infty = 4009.048$ Pa, $T_\infty = 68.33$ K, $M_\infty = 5$, and $Re/m = 37 \times 10^6$/m. Solid walls were treated as isothermal surface with a fixed temperature of $T = 300$ K. Density contours near the exit plane ($x = 0.210$ m) from Ref. [45] and present result are given in Fig. 1. The results indicated that all turbulence models used in our computational methodology can resolve global flow characteristics, no matter three shock structures in SSI or separation bubble formed by SWBLI. However, the prediction size and position of the separation bubble were unsatisfactory, which is the limitations of the RANS in handling separation [45]. Figure 2a shows pressure distributions nondimen-
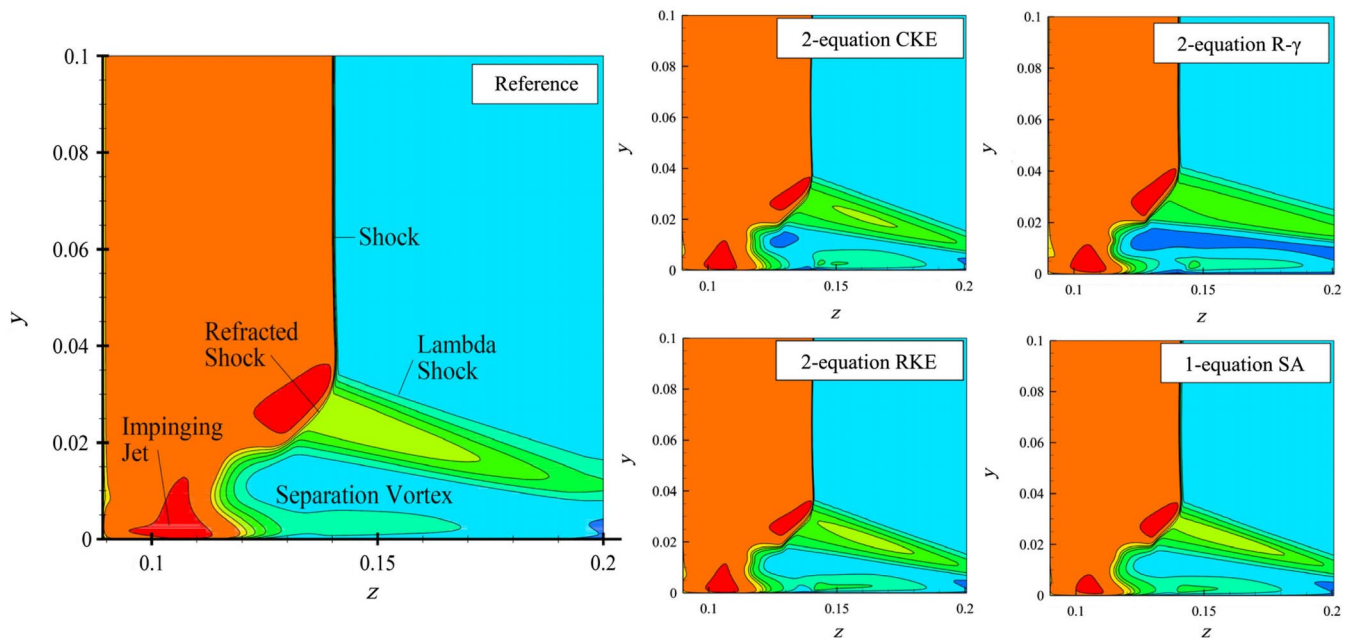

Fig. 1 Density contours of outlet plane for LF23 case ($M_\infty = 5$, $Re/m = 37 \times 10^6$/m). Left: reference CFD [45]. Right: present computation results using different turbulence models (unit: m).
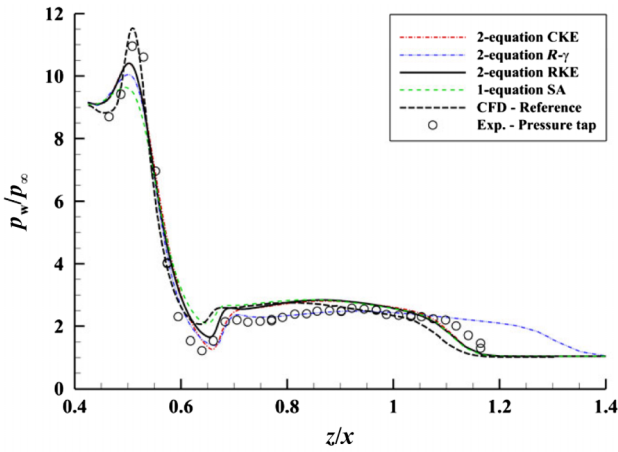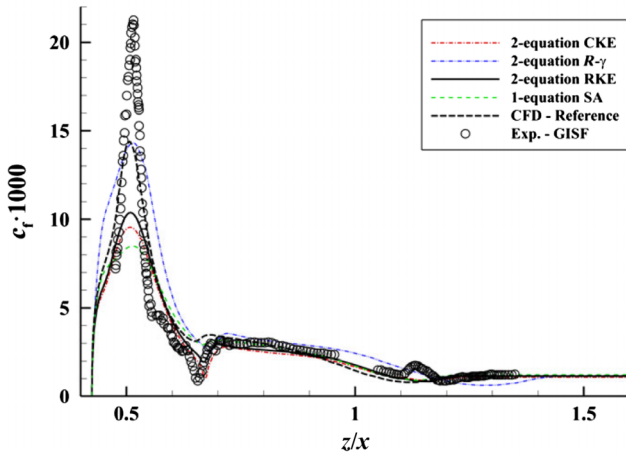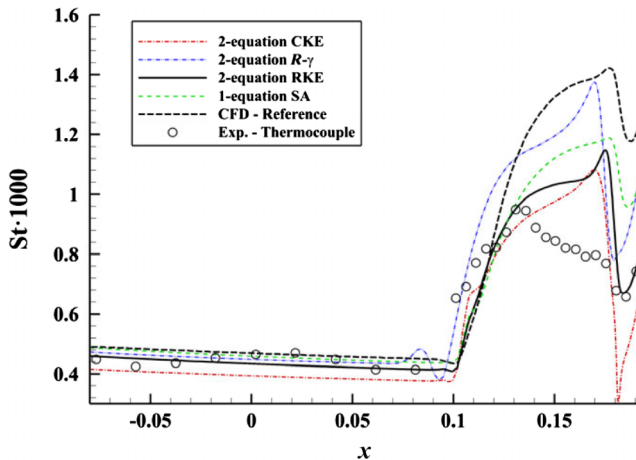
a) Wall pressure ratios along the plate at *x*=0.153m

b) Skin friction along the plate at *x*=0.122m

c) Heat flux along the plate at *z*=0.121m

Fig. 2   Comparison of distributions of aerodynamic loads for LF23 case ($M_\infty = 5$, $Re/m = 37 \times 10^6$/m) obtained by reference CFD [45], experiment [44], and present code (unit: m).

sionalized by freestream pressure at the streamwise location $x = 0.153$ m; Fig. 2b shows comparisons of measured skin friction [44] and simulation from reference computational fluid dynamics (CFD) [45] with present results. The result of surface heat flux at $z = 0.121$ m is shown in Fig. 2c. As shown in Fig. 2c, the overall trend of heat flux can be rebuilt by our computation, including the noticeable small peak just before the reattachment point. Because group of $k - \varepsilon$ turbulence model is the most commonly used and has shown satisfactory results in simulating complex flowfields of SWBLI [20,49],

RKE was used to simulate turbulence in this paper. The heat transfer peak calculated by RKE exceeds the experimental value by almost 20%. Because the purpose of this paper mainly concerns the mechanisms of heat flux distributions induced by 3-D SWBLI, the error of numerical simulation is within an acceptable range, considering the hardship in obtaining accurate heat transfer rate in both experiments and numerical simulation. The code validation shows that the numerical solver used in this paper can well capture the typical structures of flowfield and distribution trend of surface aerodynamic loads.

C.   Boundary Conditions

The physical model used in this paper is shown in Fig. 3. The computation zone obtained from the region of wing/body junction and the mounted wing was 80 mm wide, 280 mm high, and 560 mm long. Radius of wing leading edge was $R = 10$ mm. The origin of the coordinate system was set at the apex of wing blunt leading edge, where Z, X, and Y denote the spanwise, streamwise, and transverse directions, respectively. The inlet of the computation zone was at $X = -51R$. The outlet was at $X = 56R$, and the height of the region of computation, $h = 60R$, was almost two times the height of the wing.

Freestream conditions applied in this paper are listed in Table 1. It shows ground test parameters of a general shock tunnel. To save computing resources, a profile containing the boundary layer and shock parameters was imposed at the boundary of the inflow. The flowfield of the aircraft's precursor under the same freestream conditions was computed, including flow and turbulence variables. These variables were set at the inlet of the wing/body-shock interaction. Boundary specifications are also shown in Fig. 3. The boundary conditions were set to user-defined inflow and outflow at the left and right, of the computational domain, respectively. The top boundary of the domain was treated as inflow initialized by freestream conditions listed in Table 1. The boundary on the side of the symmetrical plane of the wing was treated as symmetry plane, whereas the boundary on the opposite side of the symmetry plane was set to outflow. Nonslip and isothermal conditions were used for the solid wall at a fixed temperature of 300 K.

D.   Independence Study

The numerical mesh used in this study was a fully hexahedral structured gird composed of five blocks, displayed in purple, yellow, green, blue, and orange in Fig. 4. Mesh resolution, especially the cell spacing near the wall, is critical for the prediction of surface heat transfer rate [50]. Four sets of grids (grids 1–4) were generated to study the influence of grid refinement on the solution; the details of these grids are exhibited in Table 2. N_Z, N_X, and N_Y are the number of cells in the Z, X, and Y directions, respectively. The refinements were mainly performed near the wall. There are four levels of resolutions of the grids, namely, coarse grid (grid 1), middle grid (grid 2), fine grid (grid 3), and refined grid (grid 4); the count of grids in the near-wall layer is gradually encrypted to 75, 100, 125, and 150, respectively. Although the strongest 180% increase in the grid counting in a 3-D mesh is not very convincing for the purpose of testing grid independence, grid density was increased mainly in the near-wall region of the normal direction, to make the most effective use of the limited number of grids and balance cost. The distributions of the surface pressure and heat flux on the outlet ($X/R = 56$) of the solid surface for various grid resolutions are shown in Fig. 5. Profiles of pressure and heat flux calculated by the four grids were nearly identical. The mesh resolution of grid 2 was used for the rest of this study to balance accuracy and computing resources.

One thing that must be clarified is, as shown in Fig. 5b, the profile of heat flux exhibited a rapid rise-up and fall-down at the edge of wing blunt leading edge ($Z/R \sim 1$) and junction between body and wing ($Z/R \sim 8$), marked as "cusp" and "gap" in Fig. 5b. This phenomenon mainly results from the problem of the mesh distribution at the corner. The drop of heat flux at the wing/body juncture was partly driven by physical mechanisms, because a thin streamwise vortex would form
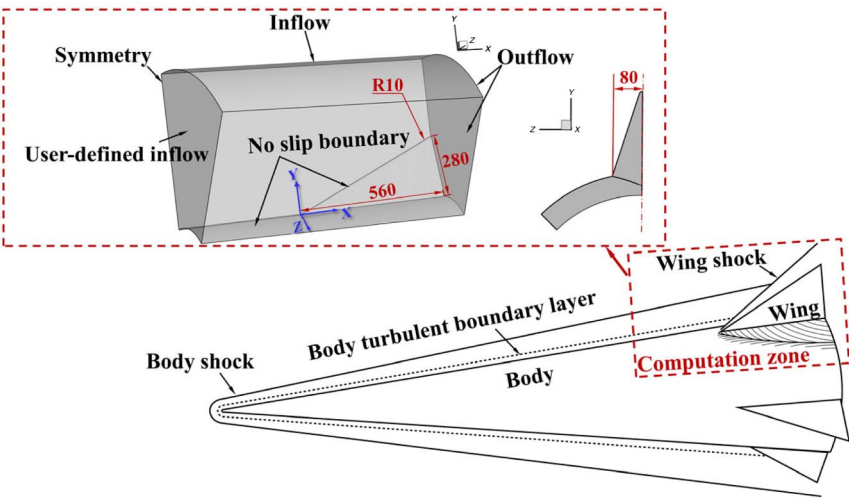
Fig. 3 Schematic and geometry of wing/body structure (unit: mm).

Table 1 Properties of freestream

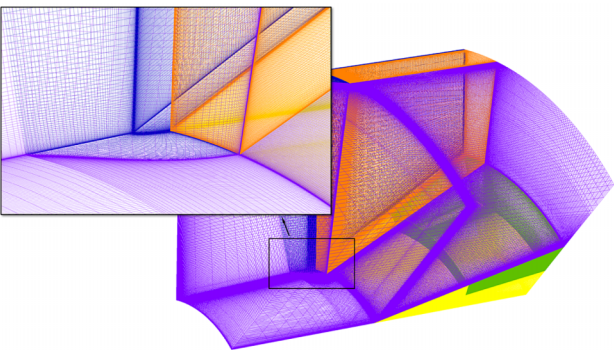| Condition	p_∞, Pa	T_∞, K	Ma	$Re \times 10^7/$m
Ground test	803.9	46.4	10	2.835

Fig. 4 Global mesh topology and magnified view of leading edge of wing mesh.

at the corner as a result of the viscous interactions between boundary layers of two surfaces.

A comparison between aerodynamic loads predicted by different turbulence models is provided in Fig. 6. It can be seen from Fig. 6 that prediction of surface pressure is insensitive to turbulence models compared with heat flux. The differences of heat flux calculated by different turbulence models mainly appear in the magnitude, and the distribution trend is similar.

III. Results and Discussion

The key results of this paper are shown in Fig. 7, which is also a roadmap for discussion of the findings. Depending on the intensity and relative position of the intersecting shock waves, i.e., body shock

and wing shock, four types of patterns of shock interactions were observed in the flowfield, as shown in the first column of Fig. 7. The flow characteristics and physics are detailed in Sec. III.A. It is well known that shock interactions inevitably cause uneven aerodynamic loads, which implies the presence of localized anomalous peak pressure and heat flux. In this paper, five profiles of the distributions of anomalous heat flux were identified according to the magnitude and position of the peaks, as shown in the third column of Fig. 7, and are discussed in Sec. III.B. To reveal the internal relationship between the distribution of heat flux and the characteristics of the flowfield of 3-D shock interactions, inspiration is drawn from Edney's work in classifying six types of two-dimensional (2-D) shock interactions. In case of 3-D shock interactions between the aircraft's body and wing, the authors extracted three mechanisms responsible for the localized peaks of heat flux: including SWBLIs, the impinging of the contact surface, and its grazing. These three mechanisms produced five kinds of local peaks in the distributions of the heat flux as five profiles. The three mechanisms are shown in the second column in Fig. 7 and are concluded in Sec. III.C.

A. Four Types of Wing/Body-Shock Interaction Patterns

Four attack angles, i.e., $\alpha = 5°$, $8°$, $10°$, and $20°$, were used to investigate how flowfield patterns and aerodynamic loads vary with the variation of pitch angles in the test conditions. The numerical results indicated that the change in angles of attack has a significant influence on the structures of the flowfield of the rear wing. Within the range of attack angles considered, the mode of wing/body-shock interaction-free, regular interaction, and Mach interaction were observed. The appearance of these different modes of interaction was dominated by the location of the initial disturbance and had a marked impact on the heat/force load distributions on the surface of the body and wing.

Figure 8 shows the flowfield patterns at the outlet as marked by the density gradient contours and dimensionless pressure distributions on the wall (left part) and sketches of the primary wave patterns in the 3-D space with a flowfield diagram of the outlet (right part). BS and WS represent detached shock waves created by the body and the wing, respectively. UWS is the undisturbed wing shock, MS is the

Table 2 Five girds used in the grid independence study

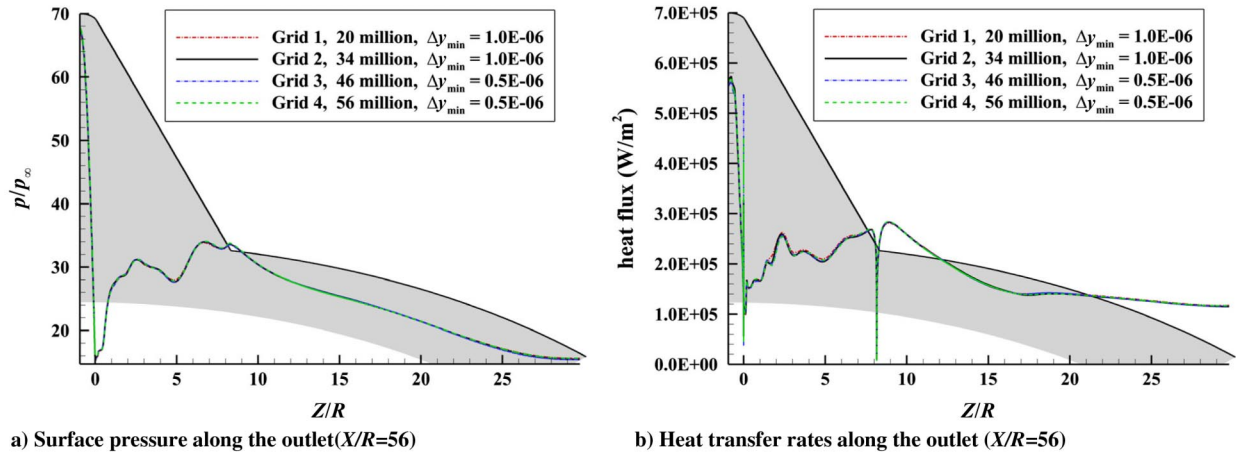|	$N_Z \times N_X \times N_Y$							
Grid	Block 1	Block 2	Block 3	Block 4	Block 5	Surface cell thickness, $\times 10^{-6}$ m	y^+	Cell count
1	$60 \times 319 \times 156$	$209 \times 194 \times 153$	$209 \times 50 \times 145$	$101 \times 351 \times 156$	$150 \times 202 \times 156$	1	<1	20 million
2	$89 \times 371 \times 181$	$269 \times 194 \times 205$	$269 \times 50 \times 145$	$101 \times 434 \times 181$	$181 \times 254 \times 181$	1	<1	34 million
3	$89 \times 396 \times 206$	$313 \times 194 \times 230$	$313 \times 50 \times 145$	$101 \times 503 \times 206$	$225 \times 279 \times 206$	0.5	<1	46 million
4	$89 \times 421 \times 231$	$359 \times 194 \times 255$	$359 \times 50 \times 145$	$101 \times 574 \times 231$	$271 \times 304 \times 231$	0.5	<1	56 million

a) Surface pressure along the outlet(X/R=56)

b) Heat transfer rates along the outlet (X/R=56)

Fig. 5   Aerodynamic loads at the outlet ($X/R = 56$) calculated by various grids.

a) Surface pressure along the outlet(X/R=56)
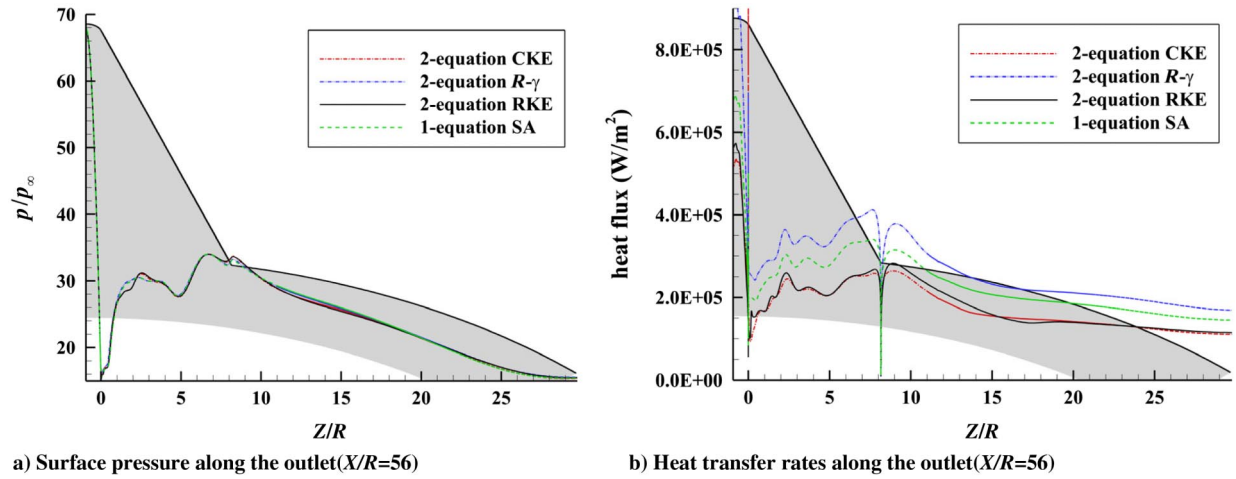
b) Heat transfer rates along the outlet(X/R=56)

Fig. 6   Aerodynamic loads at the outlet ($X/R = 56$) for grid 4 run with various turbulence models ($\alpha = 20°$).

Fig. 7   Roadmap of research and results.
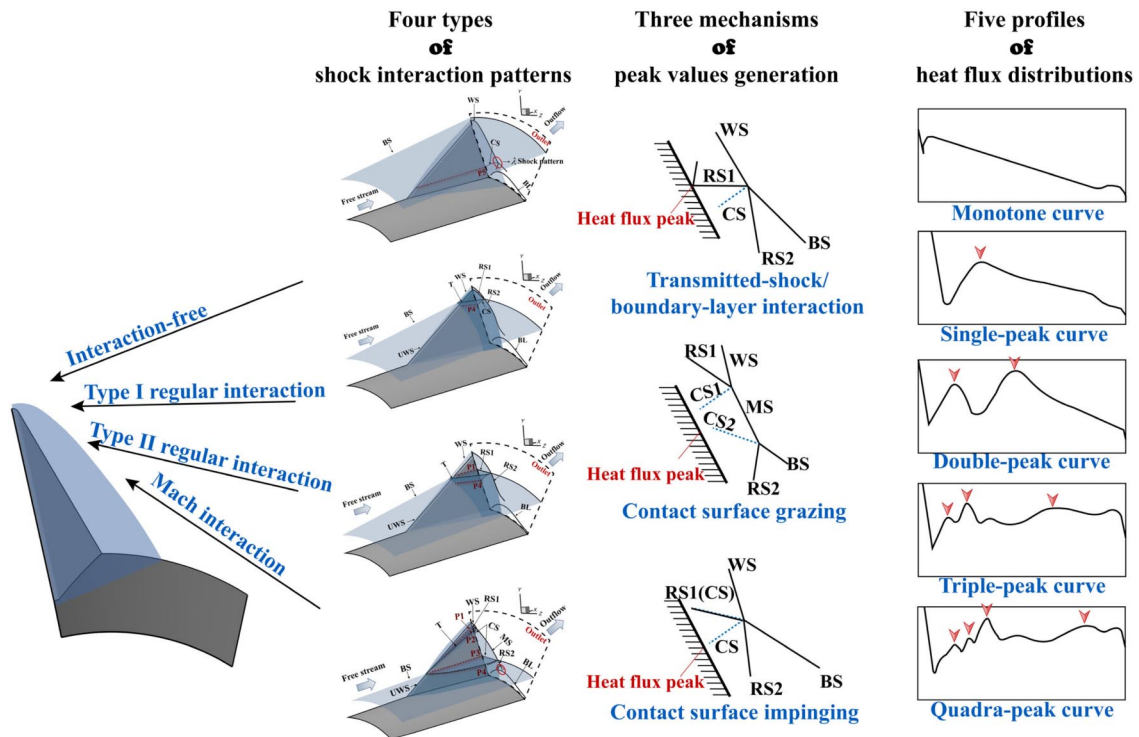
a) $\alpha = 5°$

b) $\alpha = 8°$

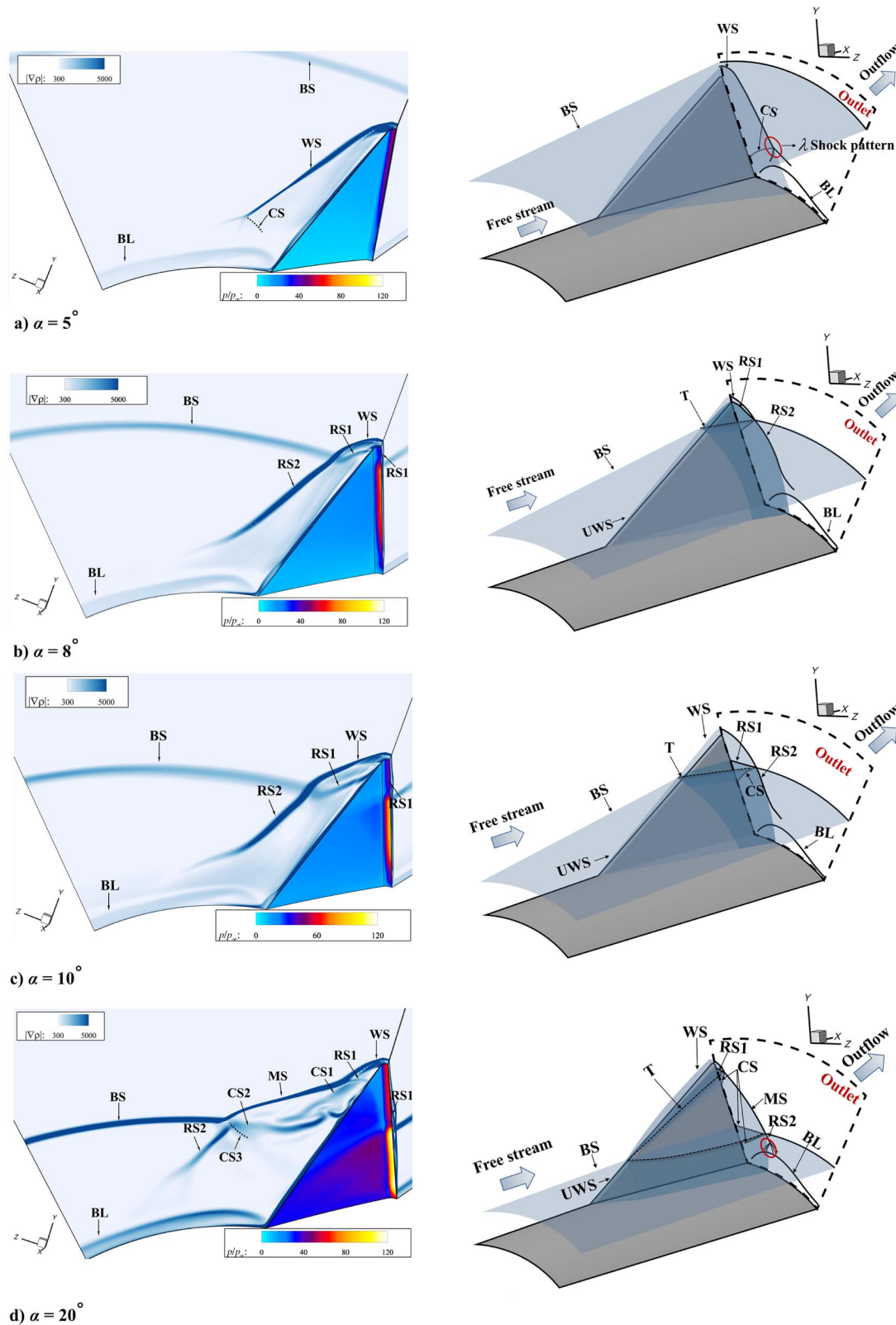c) $\alpha = 10°$

d) $\alpha = 20°$

Fig. 8 Numerical structures of the flowfield at different attack angles.

Mach stem, RS is the reflected shock wave, CS is the contact surface, and BL is the boundary layer. The line of triple points is represented by T in the figure. As is shown in Fig. 8, when the incoming Mach number was 10, minor changes in the attack angles significantly affected the mode of shock interaction, as well as the distribution of heating loads on the wall.

At $\alpha = 5°$ (see Fig. 8a), the wing shock WS did not engage in an SSI with the body shock BS; instead, a 3-D interaction between wing

shock and the boundary layer of body was observed. Owing to the stronger ability to defend separation of turbulent boundary layer than the laminar layer, the adverse pressure gradient caused by WS did not produce a boundary-layer separation, but only thickened the localized boundary layer and formed a physical "bulge" that blocked flow. As a result, a weak separation shock and a reattachment shock formed the upstream and downstream of the bulge, respectively. Together with the wing shock WS, they produced a λ shock structure similar

with that in the 2-D SWBLI. The contact surface CS induced by 3-D shock interactions represented the direction of local flow. It acted like a flow jet inclined to the wing surface and caused high, localized aerodynamic heating loads. In this case, the flow characteristics were dominated by the SWBLIs.

As the attack angle increased above 8°, wing/body shock began to interfere with each other, as shown in Figs. 8b–8d. At medium attack angles, i.e., $\alpha = 8°$ and $10°$, the regular interaction occurred (see Figs. 8b and 8c). Based on whether the reflected shock RS1 completely swept over the blunt leading edge of the wing, two types of regular interactions were observed. For type I (see Fig. 8b), the initial disturbance was located farther along the X direction and was close to the apex of the wing in the Y direction; as a result, RS1 completely swept over the apex of the wing, like a "triangular hat" on top of it. In this mode of interaction, RS1 was a conical shock. For type II (see Fig. 8c), the initial interaction occurred earlier in the X direction and later in the Y direction. As a result, the reflected shock RS1 covered only part of the leading edge of the wing, and appeared as a plane shock. When SSI occurred, the flowfield was divided into two parts according to the initial point of disturbance. Before the disturbance, the wing shock WS was buried below the body shock BS, and the flowfield was dominated by the 3-D SWBLI. The reflected shock RS was incident on the boundary layer of the body and induced a λ shock structure. Behind the initial disturbance, WS was higher than BS and generates 3-D SSI with BS. In this condition, the effects of the SSI and SWBLIs were coupled.

When the attack angle was 20° (see Fig. 8d), a 3-D Mach reflection wave configuration was obtained that generated a Mach stem (MS) bound with lines of triple points T1 and T2 as well as two contact surfaces CS1 and CS2. CS2 flowed toward the surface of the wing, which implied flow jet grazing on its boundary layer. As a result, the local boundary layer became thinner and a region of high heat flux was developed. Unlike contact surface CS2, CS1 was in the opposite direction and did not hit the surface. Mach interactions occurred at a large attack angle or high-freestream Mach numbers as BS lays close to the surface of the fuselage. The contact surface CS was induced from triple point line T, and represented the direction of local flow. Once this was pointed at the wing, a flow jet formed and would lead to a thinner local boundary layer that motivated peaks of the localized heat flux, as shown by CS in Fig. 8d.

B. Five Profiles of Rates of Distribution of Anomalous Heat Transfer

Figures 9–13 show five patterns of heat flux distribution observed in the flowfield of wing/body-shock interactions. To describe the amplification of pressure and heat flux, pressure p and heat flux q were nondimensionalized by the stagnation point values p_0 and q_0 of a blunt cone with the same head radius as the leading edge of

wing, i.e., $R = 10$ mm, under the same freestream conditions. The discussion of distribution of aerodynamic load on the wall surface was divided into three parts, i.e., wing side, blunt leading edge of the wing, and fuselage surface, to explore how the flow characteristics affected heating load on the surface.

Along the side wall of wing surface, five profiles of anomalous rates of heat flux distribution were recorded and identified as follows: monotone curve (see Fig. 9c), single-peak curve (see Fig. 10c), double-peak curve (see Fig. 11c), triple-peak curve (see Fig. 12c), and quadra-peak curve (see Fig. 13c). The monotonic curve exhibited a clean flowfield, where wing/body-shock interaction did not occur. In this case, the heat flux of wing exhibited a uniform distribution (see Fig. 9a). Along the aerodynamic load distribution on the wing surface (see Fig. 9c), the rate of heating decreased almost monotonically as no significant external flow affected the distribution. Although the overall trend of the monotonic curve was subsiding, a gentle peak occurred near the wing root, which is marked as P5 in Fig. 9c. It was produced by the contact surface CS induced from the triple point T in Fig. 9b. In addition to this, the viscous interaction of boundary layers between fuselage and wing may increase the value of heat flux in this position. Similar local peaks of heat flux appeared near the root of the wing, presenting a slight rise on the left of the gap in other profiles (see Figs. 10–13c). The interactions between the reflected shock RS and the boundary layer BL in regular interaction of wing/body shock were weak (see Figs. 10–11a). Although the λ shock structure can be extracted from the flowfield of Mach interaction (see Figs. 12–13a), it located rather far from the wing surface. In this way, the rise of heat flux near wing root was more likely due to the viscous interaction of boundary layer. Therefore, P5 is indicated only in the monotonic curve. As is shown in Figs. 14a–14e, the shock-interaction-free mode was contained in all cross sections along the direction of flow at $\alpha = 5°$. Thus, a monotonic curve representing the distribution of heat flux was maintained over the entire flowfield at $\alpha = 5°$ (see Fig. 14f). For other angles of attack, once the pattern of shock interaction had been set up and the clean flowfield was contaminated, the monotonic curve was no longer maintained, and switched to single-peak curve, as shown in Fig. 14f. This switch occurred at $X/R = 56, 45$, and 33 at attack angles of 8°, 10°, and 20°, respectively (see Figs. 14c–14f).

In case of a single-peak curve (see Fig. 10c), a local peak P4 was reached immediately downstream of the blunt leading edge due to impingement of the contact surface CS induced by regular shock interaction. As shown in Fig. 10b, CS represented a flow jet stagnated on the surface and produced a localized high pressure and heat flux. Similar flow structures appeared in Mach interaction flowfield (see CS3 in Figs. 12–13b), with the difference that the contact surface CS3 induced by matching flow parameters after triple point T2, and P4
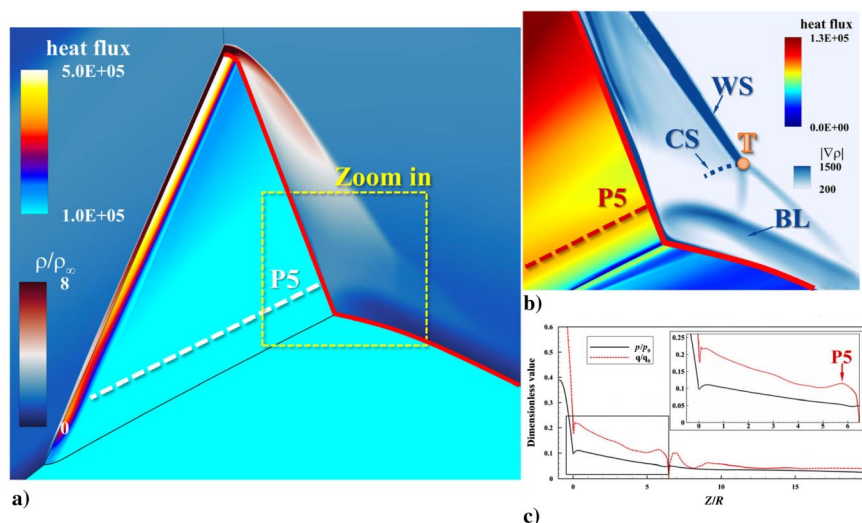

Fig. 9 Monotone curve. a) Corresponding overall flow features ($X/R = 45$ at $\alpha = 5°$). b) Enlarged section. c) Distribution of dimensionless pressure and heat flux on the surface along the red line in a).
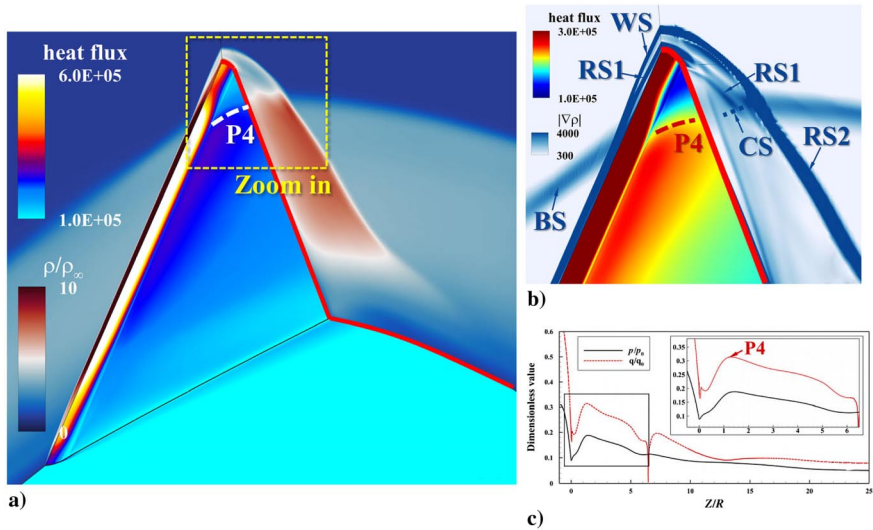
Fig. 10 Single-peak curve. a) Corresponding overall flow features ($X/R = 45$ at $\alpha = 10°$). b) Enlarged section. c) Distribution of dimensionless pressure and heat flux on the surface along the red line in a).
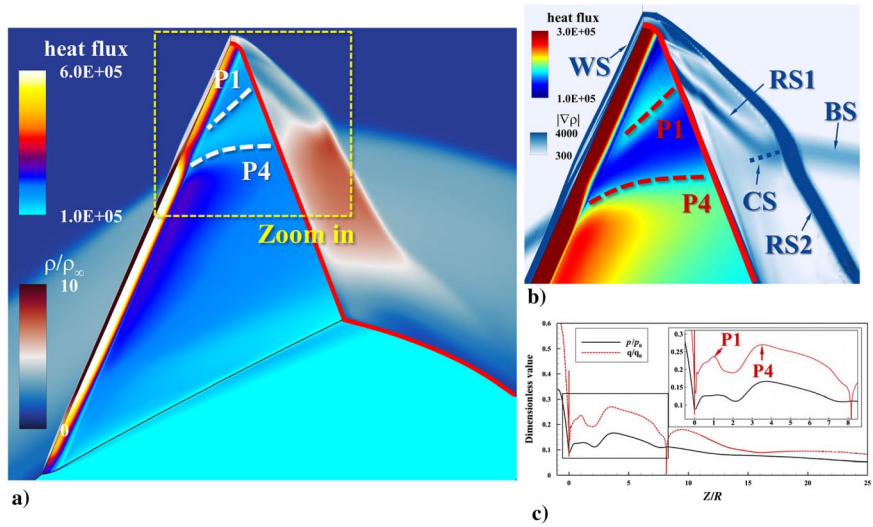

Fig. 11 Double-peak curve. a) Corresponding overall flow features ($X/R = 56$ at $\alpha = 10°$). b) Enlarged section. c) Distribution of dimensionless pressure and heat flux on the surface along the red line in a).
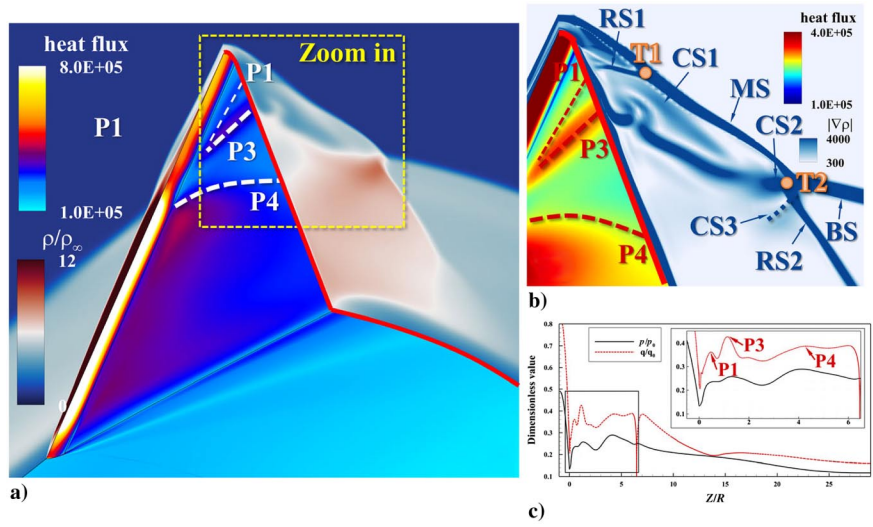

Fig. 12 Triple-peak curve. a) Corresponding overall flow features ($X/R = 45$ at $\alpha = 20°$). b) Enlarged section. c) Distribution of dimensionless pressure and heat flux on the surface along the red line in a).

was located near the root of the wing. The single-peak curve occurred when reflected shock RS1 completely swept over the wing, which was contained over the entire field of the type I regular interaction (see Figs. 14a–14e). Hence, the single-peak curve was the only non-monotonic curve appeared at $\alpha = 8°$ (see Fig. 14f). In the type II regular interaction (see Fig. 8c) and the Mach interaction mode (see Fig. 8d), the flow characteristics prevailed momentarily and the

single-peak curve occurred in a finite portion of the flowfield, that is, $X/R = 45$ at $\alpha = 10°$, and $X/R = 33$ at $\alpha = 20°$ (see Fig. 14f).

When reflected shock RS1 impinged directly on the surface of the wing instead of sweeping over it, another peak, P1, raised and formed the double-peak curve together with P4 (see Fig. 11c). P1 was caused by an SWBLI. The double-peak curve appeared only in the flowfield of type II regular interaction (see Fig. 14f at $X/R = 56$).
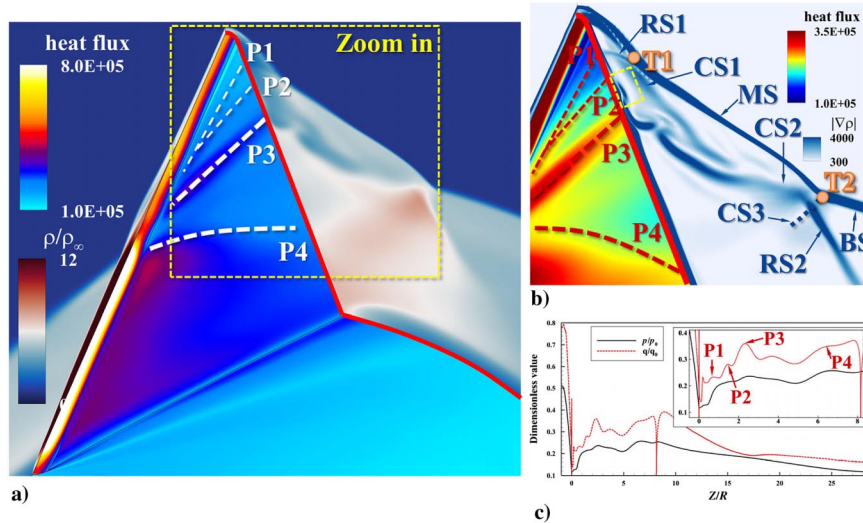

Fig. 13   Quadra-peak curve. a) Corresponding overall flow features ($X/R = 56$ at $\alpha = 20°$). b) Enlarged section. c) Distribution of dimensionless pressure and heat flux on the surface along the red line in a).

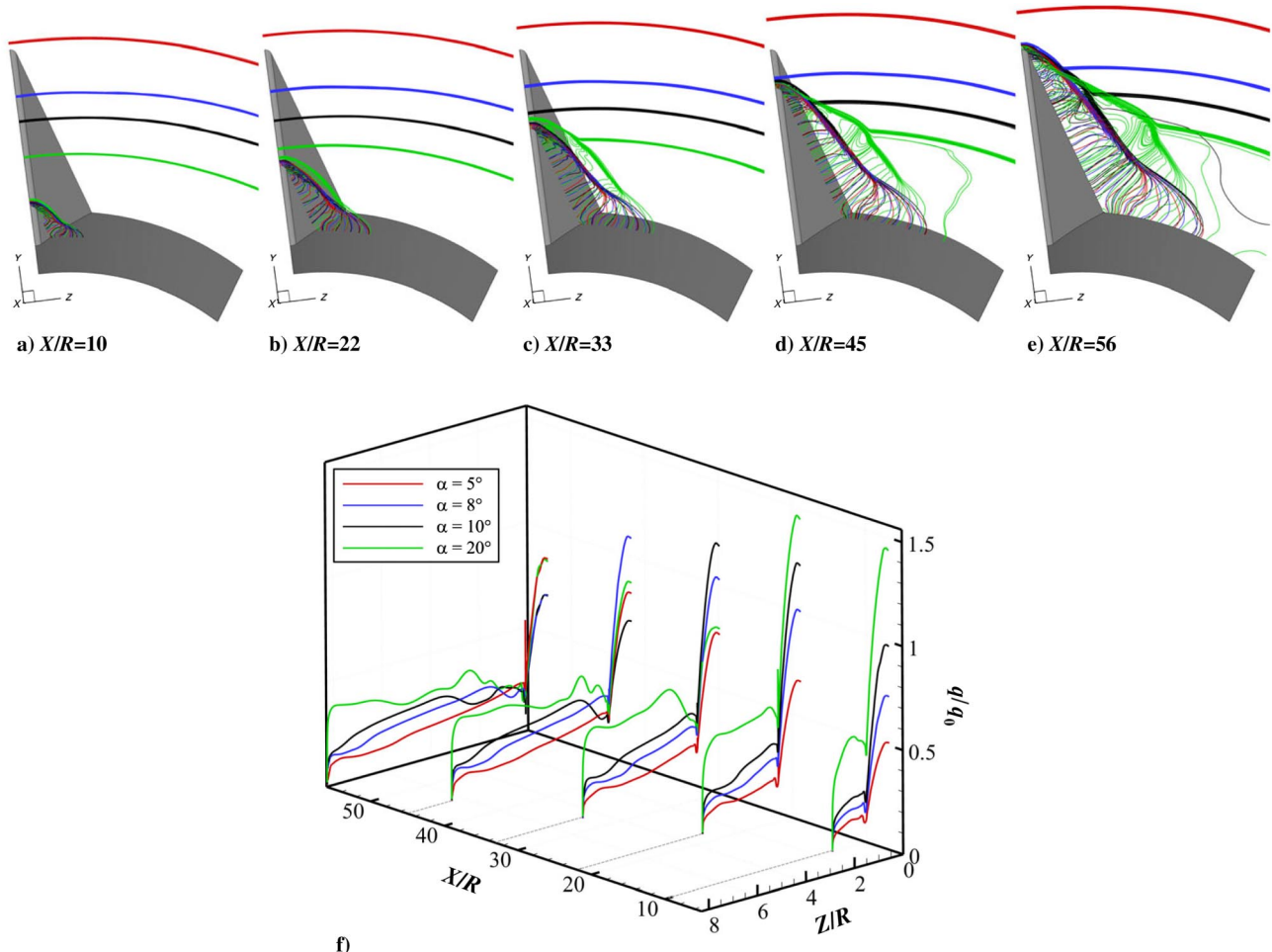a) X/R=10   b) X/R=22   c) X/R=33   d) X/R=45   e) X/R=56

f)

Fig. 14   Wave structures and dimensionless heat flux distributions of different sections along the direction of flow. a–e) Wave structures of $X/R = 10, 22, 33, 45,$ and 56 along the direction of flow. f) Dimensionless heat flux distribution of different sections on the surface of the wing.

In the Mach interaction mode, two other peaks, P2 and P3, appeared on the upper portion of wing. In the triple-peak (see Fig. 12c) and quadra-peak curves (see Fig. 13c), P3 was caused by the grazing of the contact surface CS2 conduced from the triple point T2 (see Figs. 12–13b). However, why P2 appears remains unclear. The appearance of P2 may be related to a small bulge of boundary layer around P2, which is marked with a yellow dotted box in Fig. 13b. The impingement of contact surface CS2 causes the boundary layer around P3 to be very thin and pushes fluid outward. Flow expanded around the bulge and reattached near P2, causing local heat flux to rise, as the enhancement of the heat flux results from thinning of boundary layer [25]. Besides, there is a slight expansion process of boundary layer downstream of the impingement of contact surface CS2, and a general heat flux rise downstream P3, which can be seen from Fig. 12–13c. As Fig. 14f shows, the triple-peak and quadra-peak curves appeared at $X/R = 45$ and $X/R = 56$ at $\alpha = 20°$, respectively.

Compared with the distributions of heat flux on the side wall of the wing, those on its blunt leading edge were simple. The distributions of heat flux and pressure at the center line of the leading edge are shown in Fig. 15. The interactions between the body shock and the wing shock produced two peaks in the distribution of heat flux. The sharp rise occurred due to the grazing of the contact surface, and the latter, gentler one appeared when the reflected shock swept over the wall. It can be seen form Fig. 15 that with the increment of attack angles, the body shock BS approached the wing surface and created a harsher thermal environment on the blunt leading edge. There was a rapid pressure and heat flux rise at the beginning of the leading edge, which was produced by interactions between the boundary layer of fuselage and wing shock wave. As shown in Fig. 16, the incoming boundary layer interacted with the wing shock wave and set up a regular pattern of interaction. The contact surface CS induced

from the point of intersection grazed on the leading edge of the wing and induced the first rise of heat flux shown in Fig. 15b. The 3-D streamlines around the leading edge and the limiting streamline distributed on the surface are also shown in Fig. 16. As shown in Fig. 16, the adverse pressure gradient induced by WS affected the upstream flow through the subsonic part, which occupied a small portion of the boundary layer. Therefore, the disturbance traveled upstream for a short distance and the boundary layer did not separate as much as laminar flow. As a result, the flow moved downward and rolled up again, forming a horseshoe vortex ahead of the wing and propagated downstream.

The heat flux distribution on the surface of fuselage reflected the typical quasi-conical [18,20,29] characteristics of SWBLIs (see Figs. 9–13a). On the trace of the reflected shock, where boundary layer was thickened under the adverse pressure gradient, the heat flux decreased. On both sides of the trace, the heat flux rose slightly on account of a thinner boundary layer, similarly to the separation and reattachment lines of a separated boundary layer.

C. Three Mechanisms of Peak Values Generation

In summary, three mechanisms were responsible for the intense increase in pressure and heat flux on the surface of aircraft. The peak value P1 was produced by the reflected shock/boundary-layer interaction. Peak values P4 and P5 were induced by impinging contact surfaces, and peak value P3 was related to the grazing of contact surface against the wall. Although both the second and third mechanisms were related to the impact of the contact surface, the differences were in the angles at which the contact surfaces interacted with the wall. An impinging surface connected at an almost vertical angle with the wall. Flow stagnated on this area and its influence mainly manifested as a rise in pressure, which in turn lead to a high heat flux. The contact surface grazed the wall at a small angle. It
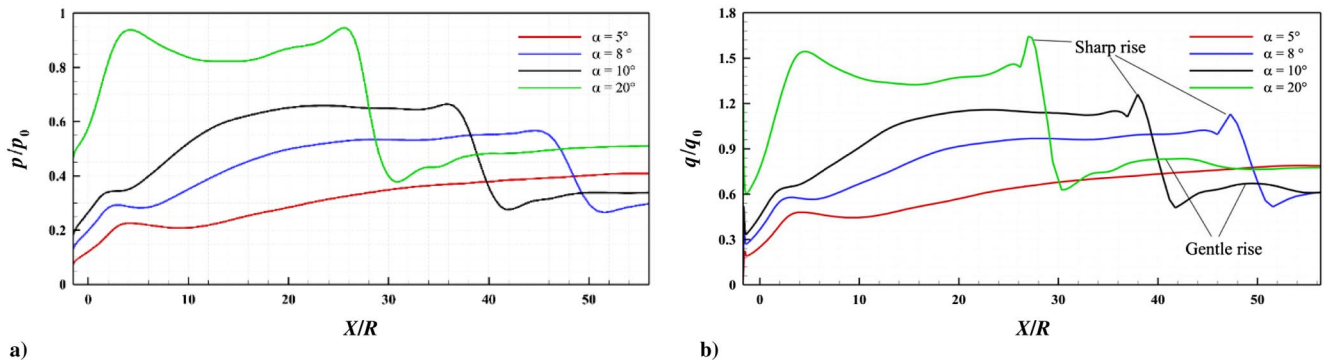

Fig. 15 Distributions of dimensionless pressure (a) and heat flux (b) on the blunt leading edge of the wing.
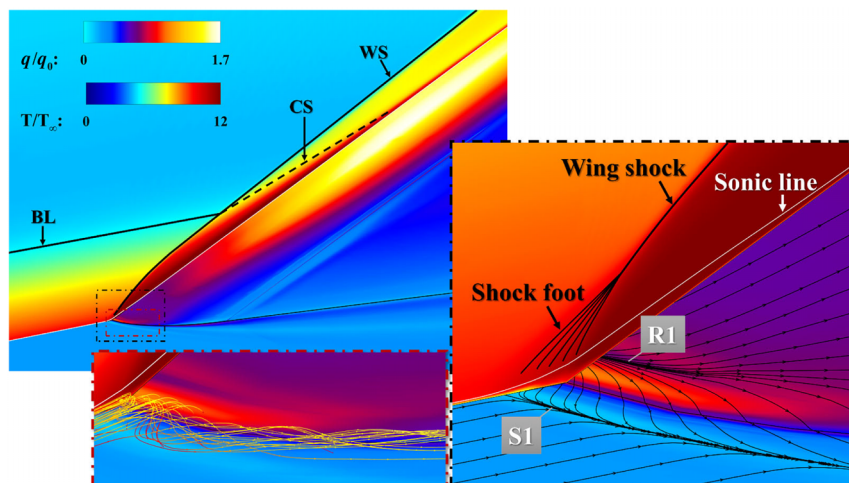

Fig. 16 Enlarged flow structures around the leading edge of the wing.

pushed away the low-velocity fluid near the wall and made the boundary layer covering surface to be very thin to induce localized heat flux peaks. Why P2 appears remains unclear and needs further study. It seems that the sudden thinning of the local boundary layer may be the main reason.

IV. Conclusions

This paper investigated the flow characteristics and aerodynamic load distributions of 3-D SSIs and SWBLIs at the junction of the body and wing of an aircraft. The shock interaction creates complex wave patterns and causes uneven distributions of heat flux on the surface of the craft. The internal relationship between the complex flow characteristics and abnormal heat flux distributions on the surface was examined and discussed in detail. The following conclusions were obtained:

1) The structures of wing/body-shock interactions varied greatly under different test conditions. Four types of shock interactions in the flowfield were observed when the attack angle changed by 15° at Mach number 10: interaction-free, type I regular, type II regular, and Mach interactions.

2) The characteristics of complex flow in the flowfield of shock interaction produced uneven heat flux distributions on the wall, and they caused localized and abnormally high heat flux zones. The Mach interaction presented the most complex flowfield structure, generating more than four local heat flux peaks along the surface of the wing of the aircraft. Because of the complex spatial characteristics of the flowfield of 3-D shock interaction, profiles of surface heat flux distribution along different directions of flow were different, relying on whether new flow structures interfered with the wall to generate respective localized peaks of heat flux.

3) Three mechanisms, reflected SWBLI, contact surface impinging, and contact surface grazing, cause the surface heat flux to increase abnormally. Of them, the contact surface grazing the wall generated the most severe localized thermal environment.

Acknowledgments

References

[1] Smith, L., Craig, K. J., Meyer, J. P., and Spedding, G. R., "Numerical Investigation of the Aerodynamic Performance for an Alternative Wing–Body–Tail Configuration," *Journal of Aircraft*, Vol. 56, No. 1, 2019, pp. 250–261.
https://doi.org/10.2514/1.C034595

[2] Zhou, L., Huang, J., Gao, Z., and Zhang, W., "Three-Dimensional Aerodynamic/Stealth Optimization Based on Adjoint Sensitivity Analysis for Scattering Problem," *AIAA Journal*, Vol. 58, No. 6, 2020, pp. 2702–2715.
https://doi.org/10.2514/1.J059136

[3] Sartor, F., and Timme, S., "Delayed Detached–Eddy Simulation of Shock Buffet on Half Wing–Body Configuration," *AIAA Journal*, Vol. 55, No. 4, 2017, pp. 1230–1240.
https://doi.org/10.2514/1.J055186

[4] Simpson, R. L., "Junction Flows," *Annual Review of Fluid Mechanics*, Vol. 33, No. 1, 2001, pp. 415–443.
https://doi.org/10.1146/annurev.fluid.33.1.415

[5] Gand, F., Deck, S., Brunet, V., and Sagaut, P., "Flow Dynamics past a Simplified Wing Body Junction," *Physics of Fluids*, Vol. 22, No. 11, 2010, Paper 115111.
https://doi.org/10.1063/1.3500697

[6] Paik, J., Escauriaza, C., and Sotiropoulos, F., "On the Bimodal Dynamics of the Turbulent Horseshoe Vortex System in a Wing-Body Junction," *Physics of Fluids*, Vol. 19, No. 4, 2007, pp. 23–27.
https://doi.org/10.1063/1.2716813

[7] Gand, F., Monnier, J.-C., Deluc, J.-M., and Choffat, A., "Experimental Study of the Corner Flow Separation on a Simplified Junction," *AIAA Journal*, Vol. 53, No. 10, 2015, pp. 2869–2877.
https://doi.org/10.2514/1.J053771

[8] Togiti, V., Eisfeld, B., and Brodersen, O., "Turbulence Model Study for the Flow Around the NASA Common Research Model," *Journal of Aircraft*, Vol. 51, No. 4, 2014, pp. 1331–1343.
https://doi.org/10.2514/1.C032609

[9] Bordji, M., Gand, F., Deck, S., and Brunet, V., "Investigation of a Nonlinear Reynolds-Averaged Navier–Stokes Closure for Corner Flows," *AIAA Journal*, Vol. 54, No. 2, 2016, pp. 386–398.
https://doi.org/10.2514/1.J054313

[10] Fu, S., Xiao, Z., Chen, H., Zhang, Y., and Huang, J., "Simulation of Wing-Body Junction Flows with Hybrid RANS/LES Methods," *International Journal of Heat and Fluid Flow*, Vol. 28, No. 6, 2007, pp. 1379–1390.
https://doi.org/10.1016/j.ijheatfluidflow.2007.05.007

[11] Ryu, S., Emory, M., Iaccarino, G., Campos, A., and Duraisamy, K., "Large-Eddy Simulation of a Wing–Body Junction Flow," *AIAA Journal*, Vol. 54, No. 3, 2016, pp. 793–804.
https://doi.org/10.2514/1.J054212

[12] Apsley, D. D., and Leschziner, M. A., "Investigation of Advanced Turbulence Models for the Flow in a Generic Wing-Body Junction," *Flow, Turbulence and Combustion*, Vol. 67, No. 1, 2001, pp. 25–55.
https://doi.org/10.1023/A:1013598401276

[13] Lindrfer, S. A., Combs, C. S., Kreth, P. A., and Schmisseur, J. D., "Numerical Simulations of a Cylinder-Induced Shock Wave/Boundary Layer Interaction," *55th AIAA Aerospace Sciences Meeting*, AIAA Paper 2017-0534, 2017.
https://doi.org/10.2514/6.2017-0534

[14] Khan, J., and Ahmed, A., "Topological Model of Flow Regimes in the Plane of Symmetry of a Surface Mounted Obstacle," *Physics of Fluids*, Vol. 17, No. 4, 2005, Paper 045101.
https://doi.org/10.1063/1.1864072

[15] Khan, M. J., Ahmed, A., and Trosper, J. R., "Dynamics of the Juncture Vortex," *AIAA Journal*, Vol. 33, No. 7, 1995, pp. 1273–1278.
https://doi.org/10.2514/3.12550

[16] Watts, J. D., "Flight Experience with Shock Impingement and Interference Heating on the X-15-2 Research Airplane," NASA TM X-1669, 1968.

[17] Babinsky, H., and Harvey, J., *Shock Wave–Boundary-Layer Interactions*, Cambridge Aerospace Series, Cambridge Univ. Press, Cambridge, 2011.
https://doi.org/10.1017/CBO9780511842757

[18] Zuo, F.-Y., and Antonio, M., "Investigation of Conical Shock Wave/Boundary Layer Interaction in Axisymmetric Internal Flow," *Aerospace Science and Technology*, Vol. 106, 2020, Paper 106106.
https://doi.org/10.1016/j.ast.2020.106106

[19] Fang, J., Yao, Y., Zheltovodov, A. A., and Lu, L., "Investigation of Three-Dimensional Shock Wave/Turbulent-Boundary-Layer Interaction Initiated by a Single Fin," *AIAA Journal*, Vol. 55, No. 2, 2016, pp. 509–523.
https://doi.org/10.2514/1.J055283

[20] Lee, Y., Settles, G. S., and Horstman, C. C., "Heat Transfer Measurements and Computations of Swept-Shock-Wave/Boundary-Layer Interactions," *AIAA Journal*, Vol. 32, No. 4, 1994, pp. 726–734.
https://doi.org/10.2514/3.12045

[21] Pickles, J. D., Mettu, B. R., Subbareddy, P. K., and Narayanaswamy, V., "On the Mean Structure of Sharp-Fin-Induced Shock Wave/Turbulent Boundary Layer Interactions over a Cylindrical Surface," *Journal of Fluid Mechanics*, Vol. 865, April 2019, pp. 212–246.
https://doi.org/10.1017/jfm.2019.53

[22] Settles, G., and Lu, F., "Conical Similarity of Shock/Boundary-Layer Interactions Generated by Swept and Unswept Fins," *AIAA Journal*, Vol. 23, No. 7, 1985, pp. 1021–1027.
https://doi.org/10.2514/3.9033

[23] Mallinson, S. G., Gai, S. L., and Mudford, N. R., "The Interaction of a Shock Wave with a Laminar Boundary Layer at a Compression Corner in High-Enthalpy Flows Including Real Gas Effects," *Journal of Fluid Mechanics*, Vol. 342, No. 2, 2011, pp. 1–35.
https://doi.org/10.1017/S0022112097005673

[24] Grisham, J. R., Dennis, B. H., and Lu, F. K., "Incipient Separation in Laminar Ramp-Induced Shock-Wave/Boundary-Layer Interactions," *AIAA Journal*, Vol. 56, No. 2, 2018, pp. 524–531.
https://doi.org/10.2514/1.J056175

[25] Hung, C. M., and MacCormack, R. W., "Numerical Solution of Three-Dimensional Shock Wave and Turbulent Boundary-Layer Interaction," *AIAA Journal*, Vol. 16, No. 10, 1978, pp. 1090–1096.
https://doi.org/10.2514/3.61007

[26] Brusniak, L., and Dolling, D. S., "Physics of Unsteady Blunt-Fin-Induced Shock Wave/Turbulent Boundary Layer Interactions," *Journal of Fluid Mechanics*, Vol. 273, Aug. 1994, pp. 375–409.
https://doi.org/10.1017/s0022112094001989

[27] Dolling, D., "Blunt Fin-Induced Shock Wave/Turbulent Boundary-Layer Interaction," *AIAA Journal*, Vol. 20, Oct. 1982, pp. 1385–1391.
https://doi.org/10.2514/3.7982

[28] Hung, C.-M., and Buning, P., "Simulation of Blunt-Fin-Induced Shock-Wave and Turbulent Boundary-Layer Interaction," *Journal of Fluid Mechanics*, Vol. 154, May 1985, pp. 163–185.
https://doi.org/10.1017/S0022112085001471

[29] Guiming, T., "Heating Characteristics of Blunt Swept Fin-Induced Shock Wave Turbulent Boundary Layer Interaction," *Acta Mechanica-Sinica*, Vol. 14, May 1998, pp. 139–146.
https://doi.org/10.1007/BF02487748

[30] Mortazavi, M., and Knight, D., "Simulation of Hypersonic-Shock-Wave–Laminar-Boundary-Layer Interaction over Blunt Fin," *AIAA Journal*, Vol. 57, No. 8, 2019, pp. 1–18.
https://doi.org/10.2514/1.J057940

[31] Thivet, F., Knight, D. D., Zheltovodov, A. A., and Maksimov, A. I., "Analysis of Observed and Computed Crossing-Shock-Wave/Turbulent-Boundary-Layer Interactions," *Aerospace Science and Technology*, Vol. 6, No. 1, 2002, pp. 3–17.
https://doi.org/10.1016/S1270-9638(01)01133-6

[32] He, F., Wu, N., Ran, F., and Wang, J., "Numerical Investigation on the Transpiration Cooling of Three-Dimensional Hypersonic Inlet," *Aerospace Science and Technology*, Vol. 106, Nov. 2020, Paper 106152.
https://doi.org/10.1016/j.ast.2020.106152

[33] Wu, N., Wang, J., and Shen, L., "Numerical Study of a Three Dimensional Interaction Between Two Bow Shock Waves and the Aerodynamic Heating on a Wedge Shaped Nose Cone," *IOP Conference Series: Materials Science and Engineering*, Vol. 187, No. 1, 2017, Paper 012001.
https://doi.org/10.1088/1757-899X/187/1/012001

[34] Naidoo, P., and Skews, B., "Supersonic Viscous Vorner Flows," *Proceedings of the Institution of Mechanical Engineers*, Vol. 226, No. 8, 2011, pp. 950–965.
https://doi.org/10.1177/0954410011416709

[35] Gun'ko, Y. P., Kudryavtsev, A. N., and Rakhimov, R. D., "Supersonic Inviscid Corner Flows with Regular and Irregular Shock Interaction," *Fluid Dynamics*, Vol. 39, No. 2, 2004, pp. 304–318.
https://doi.org/10.1023/B:FLUI.0000030314.27337.6c

[36] Xiang, G., Wang, C., Teng, H., Yang, Y., and Jiang, Z., "Study on Mach Stems Induced by Interaction of Planar Shock Waves on Two Intersecting Wedges," *Acta Mechanica Sinica*, Vol. 32, No. 3, 2016, pp. 362–368.
https://doi.org/10.1007/s10409-015-0498-2

[37] Xiang, G., Wang, C., Hu, Z., Li, X., and Jiang, Z., "Theoretical Solutions to Three-Dimensional Asymmetrical Shock/Shock Interaction," *Science China Technological Sciences*, Vol. 59, No. 8, 2016, pp. 1208–1216.
https://doi.org/10.1007/s11431-016-6036-z

[38] Xiang, G., Wang, C., Teng, H., and Jiang, Z., "Investigations of Three-Dimensional Shock/Shock Interactions over Symmetrical Intersecting Wedges," *AIAA Journal*, Vol. 54, No. 5, May 2016, pp. 1–10.
https://doi.org/10.2514/1.J054672

[39] Xiang, G., Wang, C., Teng, H., and Jiang, Z., "Shock/Shock Interactions Between Bodies and Wings," *Chinese Journal of Aeronautics*, Vol. 31, No. 2, 2018, pp. 255–261.
https://doi.org/10.1016/j.cja.2017.11.012

[40] Peng, J., Luo, C. T., Han, Z. J., Hu, Z. M., Han, G. L., and Jiang, Z. L., "Parameter-Correlation Study on Shock–Shock Interaction Using a Machine Learning Method," *Aerospace Science and Technology*, Vol. 107, No. 4, 2020, Paper 106247.
https://doi.org/10.1016/j.ast.2020.106247

[41] Zhang, Z., Wen, C., Zhang, W., Liu, Y., and Jiang, Z., "Formation of Stabilized Oblique Detonation Waves in a Combustor," *Combustion and Flame*, Vol. 223, Jan. 2021, pp. 423–436.
https://doi.org/10.1016/j.combustflame.2020.09.034

[42] Lu, H., Yue, L., Xiao, Y., and Zhang, X., "Interaction of Isentropic Compression Waves with a Bow Shock," *AIAA Journal*, Vol. 51, No. 10, 2013, pp. 2474–2484.
https://doi.org/10.2514/1.J052373

[43] Goldberg, U., Peroomian, O., and Chakravarthy, S., "A Wall-Distance-Free K-E Model with Enhanced Near-Wall Treatment," *Journal of Fluid Engineering*, Vol. 120, No. 3, Sept. 1998, pp. 457–462.
https://doi.org/10.1115/1.2820684

[44] Schülein, E., and Zheltovodov, A. A., "Documentation of Experimental Data for Hypersonic 3-D Shock Waves/Turbulent Boundary Layer Interaction Flows," DLR, German Aerospace Center Rept. IB 223-99 A 26, Göttingen, Germany, March 2001.

[45] Leger, T. J., and Poggie, J., "Computational Analysis of Shock Wave Turbulent Boundary Layer Interaction," *52nd Aerospace Sciences Meeting*, AIAA Paper 2014-0951, Jan. 2014.
https://doi.org/10.2514/6.2014-0951

[46] Allmaras, S., Johnson, F., and Spalart, P., "Modifications and Clarifications for the Implementation of the Spalart-Allmaras Turbulence Model," *7th International Conference on Computational Fluid Dynamics*, ICCFD7-1902, Hawaii, July 2012, pp. 1–11.

[47] Palaniswamy, S., Goldberg, U., Peroomian, O., and Chakravarthy, S., "Predictions of Axial and Transverse Injection into Supersonic Flow," *Flow, Turbulence and Combustion*, Vol. 66, No. 1, 2001, pp. 37–55.
https://doi.org/10.1023/A:1011479002452

[48] Mani, M., Babcock, D., Winkler, C., and Spalart, P., "Predictions of a Supersonic Turbulent Flow in a Square Duct," *51st AIAA Aerospace Sciences Meeting Including the New Horizons Forum and Aerospace Exposition.* AIAA Paper 2013-0860, Jan. 2013.
https://doi.org/10.2514/6.2013-860

[49] Wright, M. J., Sinha, K., Olejniczak, J., Candler, G. V., Magruder, T. D., and Smits, A. J., "Numerical and Experimental Investigation of Double-Cone Shock Interactions," *AIAA Journal*, Vol. 38, No. 12, 2012, pp. 2268–2276.
https://doi.org/10.2514/2.918

[50] Siddiqui, M. S., Hoffmann, K. A., Chiang, S. T., and Rutledge, W. H., "A Comparative Study of the Navier Stokes Solvers with Emphasis on the Heat Transfer Computations of High Speed Flows," AIAA Paper 1992-0835, 1992.
https://doi.org/10.2514/6.1992-835

C. Wen
Associate Editor